J. Fluid Mech. (2012), *vol.* 700, *pp.* 419–440.
doi:10.1017/jfm.2012.140

Two-dimensional modal method for shallow-water sloshing in rectangular basins

M. Antuono[1]†, B. Bouscasse[1], A. Colagrossi[1,2] and C. Lugni[1,2]

[1] CNR-INSEAN, Via di Vallerano 139, 00128 Roma, Italy

[2] Centre of Excellence for Ship and Ocean Structures, NTNU, 7491 Trondheim, Norway

(Received 21 October 2011; revised 17 February 2012; accepted 7 March 2012;
first published online 1 May 2012)

A two-dimensional model for the analysis of sloshing phenomena in shallow-water conditions has been defined using Boussinesq-type depth-averaged equations. Thanks to a modal decomposition of the spatial field, the present model allows a straightforward and simple treatment of the exciting forces and can describe a generic motion. Comparisons with the experimental data available in the literature and with a smoothed particle hydrodynamics (SPH) scheme proved the proposed shallow-water model to be accurate, fast and robust.

Key words: surface gravity waves

1. Introduction

In the last ten years there has been increasing interest in the study of sloshing phenomena in finite and shallow depth conditions (Faltinsen & Timokha 2002; Hill 2003; Faltinsen 2005; Lugni, Brocchini & Faltinsen 2006, 2010*a*; Lugni *et al.* 2010*b*). Because of the major role played by nonlinearities, the evolution of waves in tanks characterized by a small filling height represents a very demanding problem for both numerical schemes and theoretical models.

Generally, analytical and numerical works concerning sloshing phenomena without breaking are developed in the framework of the potential theory and in deep and intermediate water conditions (see, for example Faltinsen *et al.* 2000; Faltinsen & Timokha 2001, 2002). In shallow-water conditions Ockendon, Ockendon & Johnson (1986) used a proper perturbation expansion to solve the Laplace equation and obtained an integro-differential equation. Their work mainly focused on the occurrence of multiple solutions, giving an explanation for bifurcation phenomena in sloshing problems. In any case, in the shallow-water regime depth-averaged models are widely used and well-established. In this context, one of the first attempts to model shallow-water sloshing is due to Lepelletier & Raichlen (1988) who numerically solved a set of Boussinesq-type equations with a linear dispersive term. These equations proved capable of describing the main features of the evolution, providing a good agreement with the experimental measurements. More recently, Hill (2003) developed a two-dimensional modal system using a similar set of Boussinesq-type equations. This system was based on a Taylor-like expansion in the neighbourhood of the first natural

† Email address for correspondence: matteoantuono@gmail.com

resonant frequency and was thought to describe the sway motion in a rectangular tank. In this case, comparisons with the experiments by Lepelletier & Raichlen (1988) were satisfactory. Incidentally, we underline that for three-dimensional sloshing problems the use of depth-averaged equations is becoming wider and wider (see, for example Pantazopoulos 1987; Ardakani & Bridges 2011*b*) due to the reduced computational costs compared to the fully three-dimensional solvers.

Following a procedure similar to Hill (2003), we have developed a modal system that is capable of describing sloshing phenomena generated by a general two-dimensional force (i.e. a motion given by the superposition of sway, roll and heave). Differently from the work of Hill (2003), the proposed model is not restricted to cases characterized by exciting forces with small deviations from the natural resonant frequency (that is, $\omega/\omega_r \ll 1$). This feature of the model is obtained by using a spatial decomposition of the flow field and corresponds to a spatial Fourier analysis of the sloshing phenomenon. Conversely, no specific assumptions are made on the time evolution of the system modes that, consequently, are free to evolve in accordance with the exciting force acting on the tank.

The inclusion of the exciting forces in the modal system is a further point of innovation of the present work. Generally, the horizontal component of that force is added to the lowest mode as a source term (see for example Hill 2003). However, this is not consistent with the spatial decomposition of the flow variables and with the adopted governing equations. In the present work we use a spatial modulating term to spread the action of the horizontal forcing throughout the mode sequence. The modal system derived from this approach is well-posed and consistent with the conservation properties of the initial set of Boussinesq-type equations.

Comparisons with the experimental measurements by Lepelletier & Raichlen (1988) proved that the proposed model accurately predicts the free-surface amplitude response operators. Concerning the local evolution, further comparisons have been made with the δ-SPH scheme described in Antuono *et al.* (2010). This is a meshless Lagrangian numerical solver suitable for modelling gravity wave propagation and free-surface flows in general (see, for example Antuono *et al.* 2011). The good agreement with the δ-SPH scheme further confirms the ability of the proposed model to describe sloshing phenomena. Moreover, its much lower computational cost makes it suitable for an initial estimate of the shallow-water sloshing features.

The paper is organized as follows: § 2 introduces the analytical modal system and provides insight into the spatial modulating term and viscous dissipation; § 3 deals with applications and validations of the model against both numerical solutions and experimental measurements.

2. The shallow-water modal system

Let us consider a rectangular tank partially filled by water with length, breadth and still water level of respectively L^*, D^* and h^* (the starred variables indicate dimensional quantities). Assuming $D^* \ll L^*$, we can approximate the tank as two-dimensional and, then, choose a frame of reference xOy like the one shown in figure 1 in which the axis origin is on the left wall of tank and at the still water depth level.

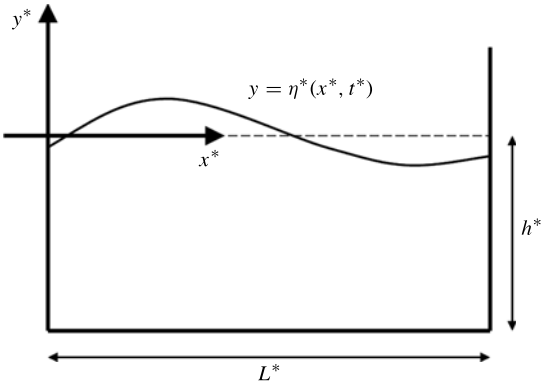

FIGURE 1. Sketch of the tank and of the frame of reference.

Further, we assume $h^* \ll L^*$, which implies that the shallow-water approximation can be adopted. Under these hypotheses, the (dimensionless) Boussinesq equations with a linearized dispersive term can be used:

$$\left.\begin{aligned} &\eta_t + u_x + (\eta u)_x = 0, \\ &u_t + u u_x + \eta_x - \frac{\mu^2}{3} u_{xxt} = 0, \end{aligned}\right\} \tag{2.1}$$

where η is the free-surface elevation, u the depth-averaged fluid velocity and $\mu = h^*/L^*$ is the dispersion coefficient. The shallow-water theory holds for $\mu < 0.1$ while for $0.1 \leqslant \mu \leqslant 0.24$ the motion is in the intermediate water depth regime (see for example Faltinsen & Timokha 2002). In the scientific literature a broad family of Boussinesq-type models exists (see for example Nwogu 1993; Gobbi, Kirby & Wei 2000; Veeramony & Svendsen 2000; Madsen, Bingham & Liu 2002). However, at the leading order all Boussinesq models prescribe the same linear dispersive term, that is, $\mu^2 u_{xxt}/3$. As pointed out in Whitham (1974), the higher-order terms neglected in the momentum equation are $O(\epsilon\mu^2, \mu^4)$ where $\epsilon = 2a^*/h^*$ is the nonlinearity parameter (a^* is the wave amplitude). Conversely, the continuity equation is exact at every order of ϵ and μ. Although the use of a linearized dispersive term may appear as a rough approximation, it allows the principal features of the sloshing motion to be retained, as shown, for example, in the works of Lepelletier & Raichlen (1988) and Hill (2003). The scaling used to make system (2.1) dimensionless is

$$x^* = L^* x, \quad t^* = \frac{L^*}{\sqrt{g^* h^*}} t, \quad \eta^* = h^* \eta, \quad u^* = \sqrt{g^* h^*}\, u, \tag{2.2}$$

where g^* is the acceleration due to gravity. At the right and left walls of the tank, the impermeability condition is imposed, that is

$$u(0, t) = u(1, t) = 0 \quad \forall t \geqslant 0, \tag{2.3}$$

and, because of the mass conservation, the following condition must hold:

$$\int_0^1 \eta(x, t)\, \mathrm{d}x = 0 \quad \forall t. \tag{2.4}$$

Assuming that the tank is subjected to a generic two-dimensional time-dependent force, the system above becomes

$$\left.\begin{aligned} &\eta_t + u_x + (\eta u)_x = 0, \\ &u_t + u u_x - F_2(t)\eta_x - \frac{\mu^2}{3} u_{xxt} = \frac{F_1(t)}{\mu}, \end{aligned}\right\} \tag{2.5}$$

where F_1 and F_2 are the horizontal and the vertical components of the global force on the tank. Explicit expressions for F_1 and F_2 are given in appendix A. As pointed out in Ardakani & Bridges (2011*a*), the dependence of the forcing term on μ^{-1} implies some restrictions on the order of magnitude of both the rotation and the horizontal component of the acceleration. Details are provided in appendix A.

Under the hypothesis that waves are non-breaking, conditions (2.3) and (2.4) are satisfied by using the following decomposition:

$$\eta(x,t) = \sum_{n=1}^{+\infty} H_n(t)\cos(n\pi x), \quad u(x,t) = \sum_{n=1}^{+\infty} U_n(t)\sin(n\pi x), \tag{2.6}$$

where $H_0 = U_0 = 0$. The series in (2.6) can be rewritten as follows:

$$\eta(x,t) = \sum_{n\in\mathbb{Z}} \frac{H_n(t)}{2}\exp(\mathrm{i}n\pi x), \quad u(x,t) = \sum_{n\in\mathbb{Z}} \frac{U_n(t)}{2\mathrm{i}}\exp(\mathrm{i}n\pi x), \tag{2.7}$$

with the conditions $H_n = H_{-n}$ and $U_n = -U_{-n}$. The use of the series in (2.7) corresponds to an expansion in Fourier modes and allows rewriting system (2.1) as a system of ordinary differential equations. Note that the present approach is totally general and partially differs from that provided by Hill (2003). In that case, a small detuning from the first natural resonant frequency of the tank was assumed and a Taylor-like expansion was performed to simplify the system of ordinary differential equations.

As shown in detail in appendix B, the decomposition in (2.7) does not allow a straightforward inclusion of the forcing term F_1 in the momentum equation. To circumvent this issue, we introduce a spatial modulation $M(x)$ as follows:

$$\left.\begin{aligned} &\eta_t + u_x + (\eta u)_x = 0, \\ &u_t + u u_x - F_2(t)\eta_x - \frac{\mu^2}{3} u_{xxt} = M(x)\frac{F_1(t)}{\mu}. \end{aligned}\right\} \tag{2.8}$$

The modulating term has to be constructed according to the decompositions in (2.7). As proved in appendix B, this implies

$$M(x) = \sum_{n=1}^{+\infty} M_n \sin(n\pi x) \quad \Leftrightarrow \quad M(x) = \sum_{n\in\mathbb{Z}} \frac{M_n}{2\mathrm{i}}\exp(\mathrm{i}n\pi x), \tag{2.9}$$

with $M_n = M_{-n}$ and $M_0 = 0$. Two conditions are required for the modulating term: one is that $M(x) \simeq 1$, the other is that the sequence $\{M_n\}$ does not modify the global amount of energy and momentum of system equation (2.5). As proved in appendix B.1, these conditions lead to

$$M_n = -2\left[\frac{(-1)^n - 1}{n\pi}\right] \quad \text{for } n \in \mathbb{Z}\setminus\{0\}, \quad M_0 = 0. \tag{2.10}$$

Specifically, the sequence $\{M_n\}$ corresponds to:

$$M(x) = \left.\begin{array}{ll} 0 & \text{if } x = 0, \\ 1 & \text{if } 0 < x < 1, \\ 0 & \text{if } x = 1. \end{array}\right\} \tag{2.11}$$

When the expressions in (2.7) and (2.9) are substituted into the Boussinesq equations, we get the following system:

$$\left.\begin{array}{l} \dot{H}_n + n\pi U_n + \dfrac{n\pi}{2}\displaystyle\sum_{p\in\mathbb{Z}} H_p U_{n-p} = 0, \\ \dot{U}_n\left(1 + \dfrac{\pi^2\mu^2 n^2}{3}\right) + n\pi F_2 H_n + \dfrac{n\pi}{4}\displaystyle\sum_{p\in\mathbb{Z}} U_p U_{n-p} = M_n \dfrac{F_1}{\mu}. \end{array}\right\} \tag{2.12}$$

For numerical reasons, it is better to make the nonlinear contributions symmetric with respect to their summations. After this has been done, the system is

$$\left.\begin{array}{l} \dot{H}_n + n\pi U_n + \dfrac{n\pi}{4}\displaystyle\sum_{p\in\mathbb{Z}} \left[H_p U_{n-p} + H_{n-p} U_p\right] = 0, \\ \dot{U}_n\left(1 + \dfrac{\pi^2\mu^2 n^2}{3}\right) + n\pi F_2 H_n + \dfrac{n\pi}{4}\displaystyle\sum_{p\in\mathbb{Z}} U_p U_{n-p} = M_n \dfrac{F_1}{\mu}. \end{array}\right\} \tag{2.13}$$

2.1. *Viscous effects*

Sloshing problems in small fluid depths are characterized by a large content of higher frequencies that correspond to higher modes. Since these modes are believed to be largely damped by energy dissipation, it is a common practice to add a damping term to the momentum equation. Similarly to the works of Faltinsen & Timokha (2001), Faltinsen, Rognebakke & Timokha (2006) (deep and intermediate water conditions) and Hill (2003) (shallow-water conditions), we use a linear viscous term, i.e. a term that is proportional to the fluid velocity. The coefficient of the viscous term (that is, the damping coefficient) is defined following the work of Lamb (1945) and Keulegan (1959). It gives the mean dissipation rate during a period of the evolution and takes into account both the dissipation in the fluid bulk and the dissipation due to the boundary layers at the tank walls.

When the viscosity term is added into the momentum equation of system (2.13), we get

$$\left.\begin{array}{l} \dot{H}_n + n\pi U_n + \dfrac{n\pi}{4}\displaystyle\sum_{p\in\mathbb{Z}} \left[H_p U_{n-p} + H_{n-p} U_p\right] = 0, \\ \dot{U}_n\left(1 + \dfrac{\pi^2\mu^2 n^2}{3}\right) + n\pi F_2 H_n + \beta_n U_n + \dfrac{n\pi}{4}\displaystyle\sum_{p\in\mathbb{Z}} U_p U_{n-p} = M_n \dfrac{F_1}{\mu}, \end{array}\right\} \tag{2.14}$$

where

$$\beta_n = \sqrt{\frac{n\pi}{2Re}}\left(1 + \frac{2h^*}{D^*}\right)\frac{L^*}{h^*} + \frac{4n^2\pi^2}{Re}, \tag{2.15}$$

and $Re = (L^*\sqrt{g^* h^*})/\nu^*$ is the Reynolds number. The first term in the right-hand side of (2.15) takes into account the dissipation due to the boundary layers while the second one describes the dissipation inside the fluid bulk.

Incidentally, we highlight that slightly different formulae for the damping coefficient have been derived in Faltinsen & Timokha (2002) and reviewed in Faltinsen & Timokha (2009).

3. Validation and applications

The model proposed in this work has been validated against experimental measurements and numerical simulations. In the latter case, we compared the theoretical model with a smoothed particle hydrodynamics (SPH) scheme. This scheme has been satisfactorily applied to sloshing problems in Souto-Iglesias *et al.* (2006), Bouscasse *et al.* (2007), Bulian *et al.* (2010) and Colagrossi *et al.* (2010). Here, we use it as a cross-check when experimental measurements are available (such as for the sway motion) and as a full comparison in those test cases (such as the roll motion) where experimental data on non-breaking sloshing phenomena are not available. The main features of the SPH scheme are reported in § 3.1. Incidentally, we highlight that all the SPH simulations shown in the following sections have reached converged solutions.

System (2.14) has been integrated in time by using a fourth-order Runge–Kutta scheme. Note that a typical SPH run employs $\sim 10^4$ particles and a simulation of 300 s of physical evolution on a single processor Xeon 2.3 GHz has a CPU time cost of $\sim$10 days. Conversely, the same case simulated through the modal system (2.14) with 30 modes and for a duration of 1000 s of physical evolution has a CPU time cost of $\sim$45 s. Such a large difference suggests that the present model can be also useful for an initial estimate of the main features of sloshing phenomena and for real-time simulations.

3.1. *The SPH model*

The SPH scheme is a meshless Lagrangian method in which the fluid domain is discretized in a finite number of particles representing elementary fluid volumes V^*, each one with its own local mass m^* and other physical properties. In this context a generic field f^* at the position $\boldsymbol{r}_i^*$ of the ith particle is approximated through the convolution sum

$$\langle f^* \rangle (\boldsymbol{r}_i^*) = \sum_j f_j^* W^*(\boldsymbol{r}_i^* - \boldsymbol{r}_j^*, \epsilon^*) V_j^*, \tag{3.1}$$

where f_j^* is the value of f^* associated with the generic particle j, V_j^* is its volume and, finally, $W^*(\boldsymbol{r}_i^* - \boldsymbol{r}_j^*, \epsilon^*)$ is a weight function that, in the SPH literature, is generally called the kernel function. The kernel function has a compact support with radius proportional to ϵ^* (also known as the smoothing length) and tends to a delta Dirac 'function' when ϵ^* goes to zero. The integration of the kernel function on its support is imposed to be equal to one. For ease of notation, hereinafter we denote $W^*(\boldsymbol{r}_i^* - \boldsymbol{r}_j^*, \epsilon^*)$ simply as W_{ij}^* and use a Gaussian kernel, as done in Landrini *et al.* (2007).

In the present work we adopt the δ-SPH scheme proposed by Antuono *et al.* (2010) and further examined in Antuono *et al.* (2011) for gravity wave propagation. In this framework, the fluid is assumed to be barotropic and weakly compressible and the reference equations for the flow evolution are the Euler equations along with a linear state equation. An appropriate artificial diffusive term is used into the continuity equation in order to remove the spurious numerical high-frequency oscillations in the pressure field and, similarly to most weakly compressible SPH schemes, an artificial viscous term is added to the momentum equation for stability reasons (see for example

Monaghan 2005). As proved in Antuono *et al.* (2010), the δ-SPH scheme satisfies the conservation of linear and angular momenta. The dimensionless δ-SPH scheme is

$$\left.\begin{aligned}
&\frac{\mathrm{D}\rho_i}{\mathrm{D}t} = -\rho_i \sum_j (\boldsymbol{u}_j - \boldsymbol{u}_i)\cdot\nabla_i W_{ij} V_j + \delta\frac{\epsilon}{M}\sum_j \boldsymbol{\psi}_{ij}\cdot\nabla_i W_{ij} V_j,\\
&\rho_i\frac{\mathrm{D}\boldsymbol{u}_i}{\mathrm{D}t} = -\sum_j (p_j + p_i)\nabla_i W_{ij} V_j + \rho_i \boldsymbol{f}_i + \alpha\frac{\epsilon}{M}\sum_j \pi_{ij}\nabla_i W_{ij} V_j\\
&p_i = (\rho_i - 1),\\
&\frac{\mathrm{D}\boldsymbol{r}_i}{\mathrm{D}t} = \boldsymbol{u}_i,
\end{aligned}\right\} \tag{3.2}$$

where ρ_i, p_i and $\boldsymbol{u}_i$ are the density, the pressure and the velocity of the ith particle while $M = \sqrt{g^* h^*}/c_0^*$ is the Mach number (c_0^* is the sound velocity). Symbol $\boldsymbol{f}_i$ denotes the dimensionless body force acting on the ith particle in the frame of reference of the tank. The scaling factors are

$$\rho^* = \rho_0^*\rho, \quad p^* = c_0^{*2}\rho_0^* p, \quad \epsilon^* = L^*\epsilon, \quad \boldsymbol{f}^* = g^*\left(\frac{h^*}{L^*}\right)\boldsymbol{f}, \tag{3.3}$$

$$V^* = V_0^* V = \left(\frac{m^*}{\rho_0^*}\right) V, \quad W_{ij}^* = \frac{W_{ij}}{V_0^*}, \tag{3.4}$$

where ρ_0^* is the reference density (that is, the density along the free surface). The arguments of the diffusive and viscous terms are

$$\boldsymbol{\psi}_{ij} = 2\left(\rho_j - \rho_i\right)\frac{(\boldsymbol{r}_j - \boldsymbol{r}_i)}{|\boldsymbol{r}_j - \boldsymbol{r}_i|^2} - \left[\langle\nabla\rho\rangle_i^L + \langle\nabla\rho\rangle_j^L\right], \quad \pi_{ij} = \frac{(\boldsymbol{u}_j - \boldsymbol{u}_i)\cdot(\boldsymbol{r}_j - \boldsymbol{r}_i)}{|\boldsymbol{r}_j - \boldsymbol{r}_i|^2}. \tag{3.5}$$

The symbol $\langle\nabla\rho\rangle_i^L$ indicates the renormalized gradient defined in Randles & Libersky (1996).

In all simulations, $\delta = 0.1$ while α changes according to the kinematic viscosity used in the SPH scheme. As shown in Español & Revenga (2003), the numerical viscous term added to the momentum equation approximates the Laplacian of the velocity for incompressible fluids. Specifically, the SPH Reynolds number for two-dimensional problems is $Re_{sph} = 8M/(\epsilon\alpha)$ (see Monaghan 2005 for more details).

To reduce the computational effort, it is a common practice in the weakly compressible SPH solvers to use a sound velocity much smaller than the physical one, generally one order of magnitude larger than the maximum expected velocity of the fluid. However, for gravity waves the flow velocity is generally small while the most important quantity associated with the wave propagation is the wave celerity, that is, $c^{*2} = g^*/k^* \tanh(k^* h^*)$ where k^* is the wavenumber (see for example Madsen & Shäffer 2006). For h^* going to zero, the shallow-water regime is approached and the relation above becomes $c^{*2} = \sqrt{g^* h^*}$. Since this expression is an upper bound for the wave celerity (that is, $g^*/k^* \tanh(k^* h^*) \leqslant \sqrt{g^* h^*}$), we choose $c_0^* = 10\sqrt{g^* h^*}$ which corresponds to $M = 0.1$.

The detection of the free surface has been obtained through the algorithm proposed by Marrone *et al.* (2010) while the solid boundaries have been modelled through fixed ghost particles as described in Marrone *et al.* (2011). Specifically, a free-slip condition has been implemented along solid boundaries and the Neumann condition has been imposed, that is $\partial p/\partial n = \rho \boldsymbol{f}\cdot\boldsymbol{n}$ where $\boldsymbol{n}$ is the normal unit vector to the solid profile pointing out of the fluid region.

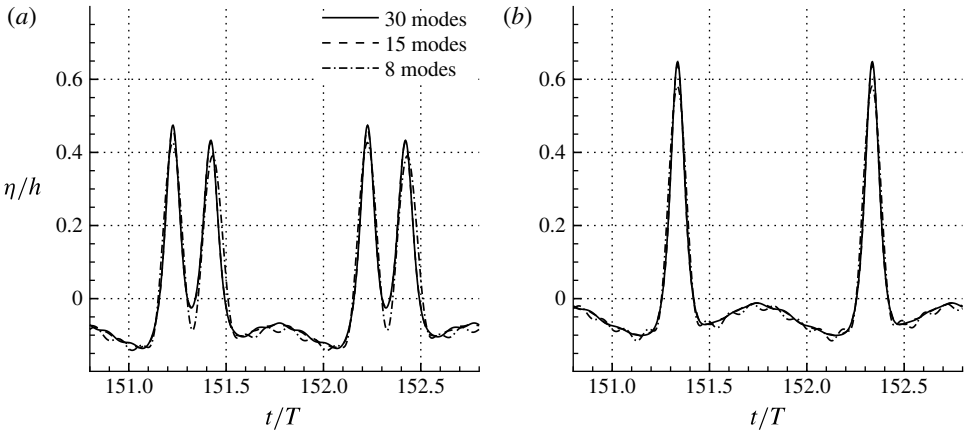

FIGURE 2. Sway motion, first configuration ($h^*/L^* = 0.051$, $A^*/h^* = 0.065$): (*a*) $\omega/\omega_r = 1.02$, (*b*) $\omega/\omega_r = 1.08$. Convergence tests for the free-surface evolution at $x^*/L^* = 1$.

As verified in Antuono *et al.* (2011), the damping coefficient of the SPH scheme is given by $\beta_{sph} = 4\pi^2/Re_{sph}$. This term has been derived from the works of Lamb (1945) and Lighthill (2001) under the assumption that the dissipation due to the boundary layer is negligible. Such a hypothesis is consistent with the fact that in all the SPH simulations free-slip conditions have been used along the tank walls. Unfortunately, it also implies that the structure of the SPH damping coefficient is different from that of the damping coefficient adopted for the modal system. In any case, to make the SPH scheme and the modal system (2.14) have approximately the same dissipation rate, we require that the order of magnitude of β_{sph} is similar to that of β_1 (see (2.15)). Generally, a good choice is $\beta_{sph} \simeq 0.2\beta_1$. This approximate expression allows the definition of the SPH Reynolds number, Re_{sph}.

3.2. *Sway motion*

Sway motion consists of a horizontal forcing while the vertical displacement and rotation are null. Specifically, we consider the experimental campaign of Lepelletier & Raichlen (1988) where two different configurations were considered. In the first case, the tank dimensions are $L^* = 117.5$ cm, $D^* = 12$ cm and the still water level is $h^* = 6$ cm The first resonant frequency predicted through the linear theory is $\omega_r^* = 2.04$ s^{-1}, the horizontal forcing law is sinusoidal and its amplitude is $A_1^* = 0.39$ cm. The kinematic viscosity is $\nu^* = 0.0094$ cm^2 s^{-1}.

For this case, system (2.14) reaches a converged solution using 30 modes (the analysis has been repeated using 8, 15 and 60 modes). All simulations have been run up to $t^*/T^* = 200$ to go past the transient regime and ensure the attainment of periodic conditions (here, $T^* = 2\pi/\omega^*$ is the period of the forcing excitation). Hereinafter, following Faltinsen & Timokha (2002) we refer to these conditions as 'steady-state conditions'. Figure 2 displays some convergence tests at the steady state for different ratios ω/ω_r. Here, simulations with 60 modes have not been shown since they are practically identical to the cases with 30 modes.

Figure 3(*a*) displays a comparison between the experiments by Lepelletier & Raichlen (1988) (triangles and thin solid line) and the present model (thick solid line) for the steady-state maximum wave elevation at the right-hand wall of the tank ($x^*/L^* = 1$). The overall agreement is very good and the bifurcation predicted by

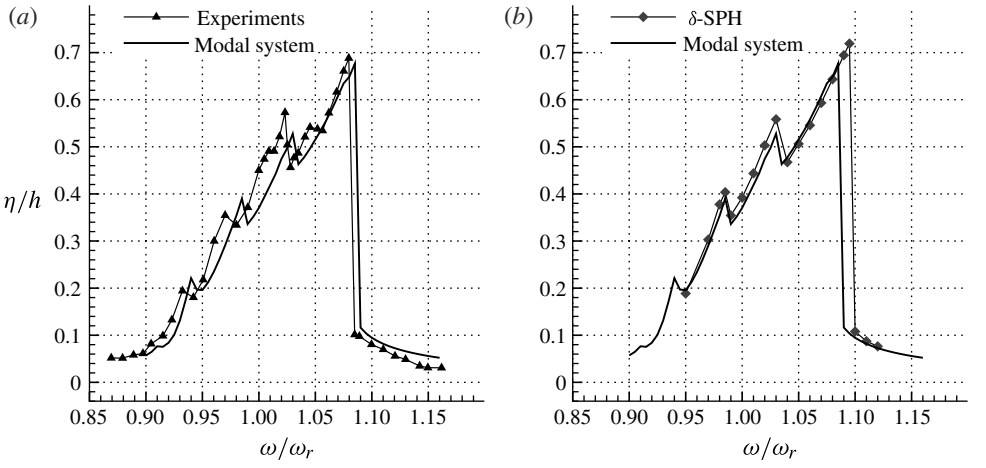

FIGURE 3. Sway motion, response amplitude operator at $x^*/L^* = 1$ for the first configuration ($h^*/L^* = 0.051$, $A^*/h^* = 0.065$).

the present model is very close to that shown by the experiments. In figure 3(*b*), system (2.14) has been compared with the results obtained through the δ-SPH scheme ($Re_{sph} = 2900$, $h/\mathrm{d}x = 50$ where $\mathrm{d}x$ is the mean particle distance). Although the SPH scheme tends to slightly delay the bifurcation, the agreement between the two models is excellent.

The small sawtooth peaks that appear along the left-hand branch of the response amplitude operator (see figure 3) correspond to the boundaries of different regimes of the sloshing evolution. Each regime is characterized by a specific number of waves and this number decreases as the peaks approach the bifurcation point (see for example Olsen & Johnsen 1975). The last regime before the bifurcation is characterized by a single-bump wave that moves back and forth in the basin. After the bifurcation, only one wave is observed. Figure 4 displays the time evolution of the free-surface elevation at $x^*/L^* = 1$ for some of these regimes. These results have been compared with the δ-SPH solver described in § 3.1 showing an excellent match with the numerical solutions.

In the second experiments, Lepelletier & Raichlen (1988) used a tank with $L^* = 60.95$ cm, $D^* = 23$ cm and $h^* = 6$ cm. The horizontal forcing amplitude was $A_1^* = 0.196$ cm and the first resonant frequency predicted through the linear theory was $\omega_r^* = 3.893\ \mathrm{s}^{-1}$. Again, system (2.14) reaches a converged solution using 30 modes and all simulations have been run up to $t^*/T^* = 200$ to ensure the attainment of steady-state conditions.

This second configuration is particularly demanding for it is characterized by $\mu = h^*/L^* = 0.098$ and, therefore, the sloshing motion is very close to the intermediate water depth regime. Lepelletier & Raichlen observed the occurrence of wave breaking during the transient evolution of those cases characterized by frequencies just to the left of the bifurcation point (that is, $\omega/\omega_r = 1.06$). However, no breaking was observed at the steady state. This is an important point since implies that the comparison with the proposed modal system is still possible. Indeed, wave breaking induces further energy dissipation with respect to the boundary layer. Since the modal system cannot model breaking waves, it is characterized by an excess of energy compared

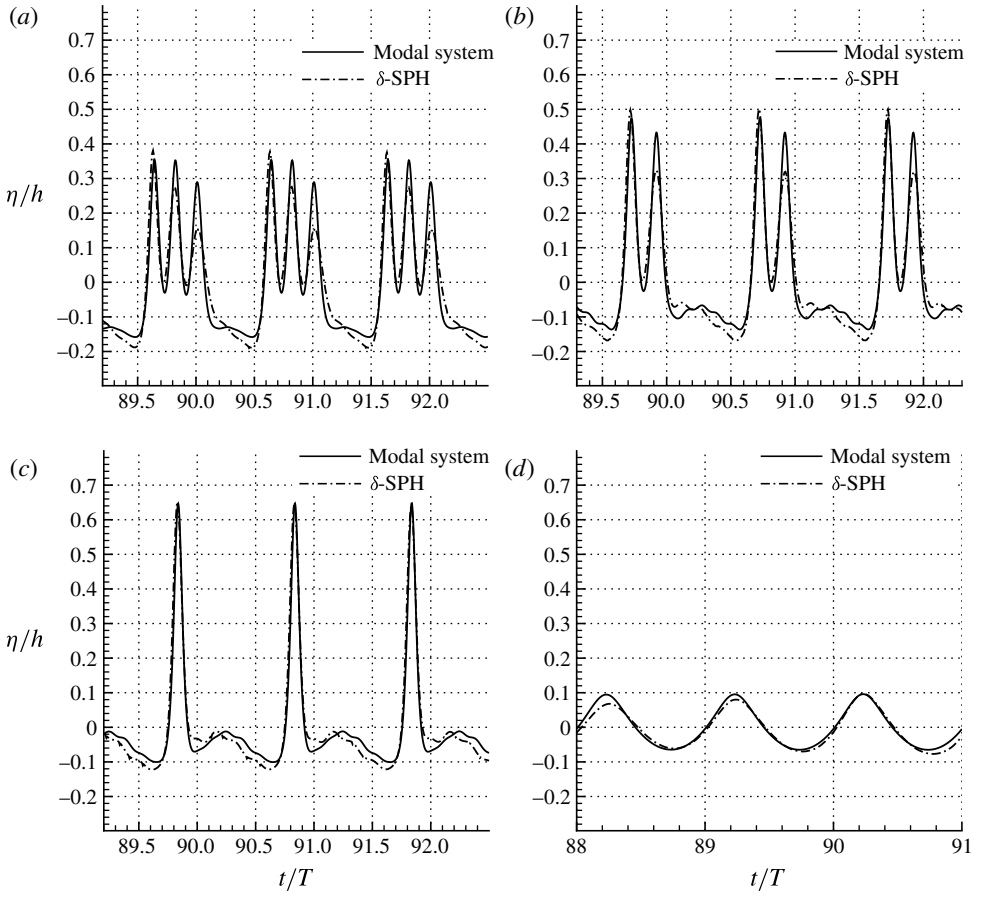

FIGURE 4. Sway motion, first configuration. Evolution of the free surface at $x^*/L^* = 1$: (*a*) $\omega/\omega_r = 0.98$, (*b*) $\omega/\omega_r = 1.02$, (*c*) $\omega/\omega_r = 1.08$, (*d*) $\omega/\omega_r = 1.10$.

to the experiments during the transitory stage. In any case, such an excess is slowly dissipated during the evolution and just leads to a delay in the attainment of the steady-state conditions (where the comparison with the experiments is possible since waves are non-breaking).

Figure 5(*a*) displays a comparison between the amplitude response operator at $x^*/L^* = 1$ as given by the experimental measures (triangles and thin solid line) and by the present model (thick solid line). The match is very good and the bifurcation point is predicted accurately. In figure 5(*b*), the modal system is compared with the δ-SPH scheme ($h/\mathrm{d}x = 60$, $Re_{sph} = 7000$). The SPH tends to overestimate the analytical model close to the bifurcation that, similarly to the previous case, is slightly delayed with respect to the experiments.

In this case only two regimes are observed before the bifurcation point: a two-wave regime and a single-bump-wave regime. These have been compared with the δ-SPH scheme in figure 6. Between these regimes a special region of motion was detected during the experimental campaign. In that region no steady state was attained and a nonlinear subharmonic modulation of 18 periods was observed (see Lepelletier & Raichlen 1988). Remarkably, system (2.14) predicts the same modulation in a

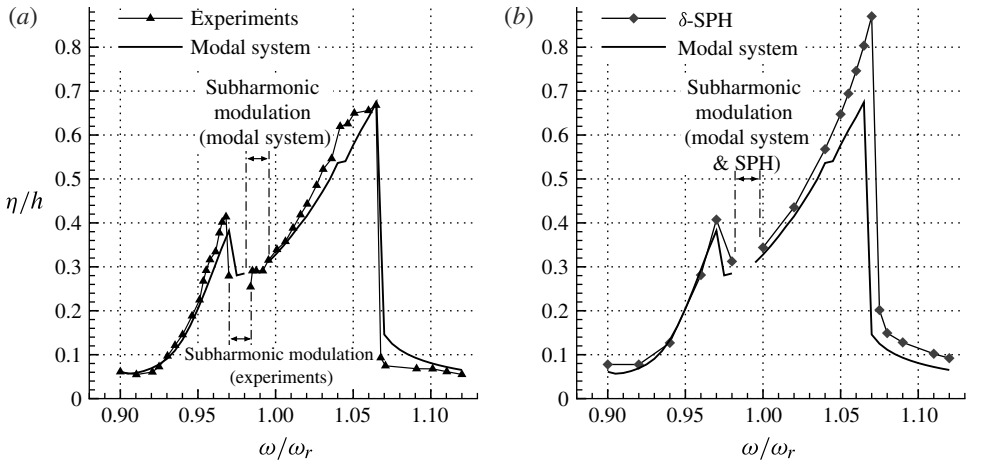

FIGURE 5. Sway motion, response amplitude operator at $x^*/L^* = 1$ for the second configuration ($h^*/L^* = 0.098$, $A^*/h^* = 0.033$).

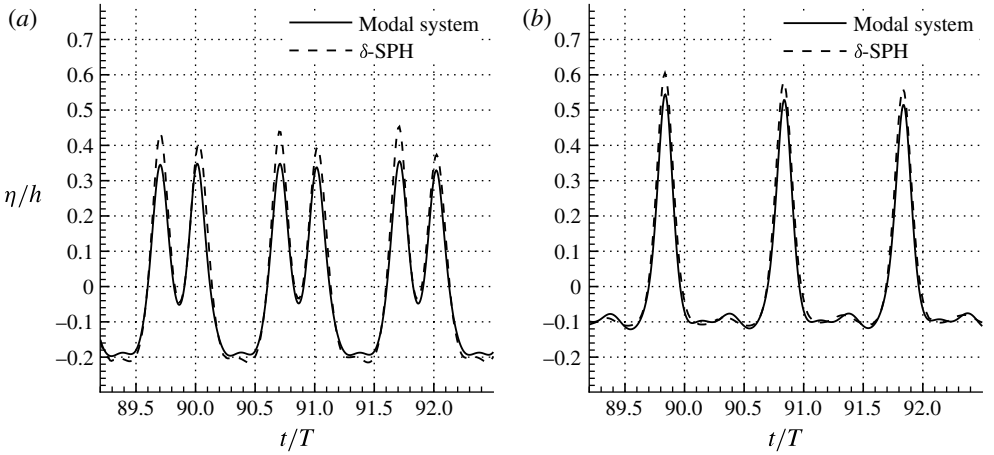

FIGURE 6. Sway motion, second configuration. Evolution of the free surface at $x^*/L^* = 1$: (*a*) $\omega/\omega_r = 0.97$, (*b*) $\omega/\omega_r = 1.04$.

region very close to that shown by the experiments (see figure 5). Details on the nonlinear beating phenomenon are provided in figure 7 and are compared with the δ-SPH scheme. In this case, very long simulations have been performed to ensure the attainment of a periodic asymptotic solution. Again, the agreement between the numerical and theoretical model is very good.

3.3. *Roll motion*

In this section we provide an example of roll motion using the modal system (2.14). Owing to the difficulty in finding experiments where no breaking events occur, we just provide comparisons with the δ-SPH model. To this purpose and because of the no-slip conditions implemented by this model, we neglect the component of the damping coefficient β_n which comes from the boundary layer dissipation

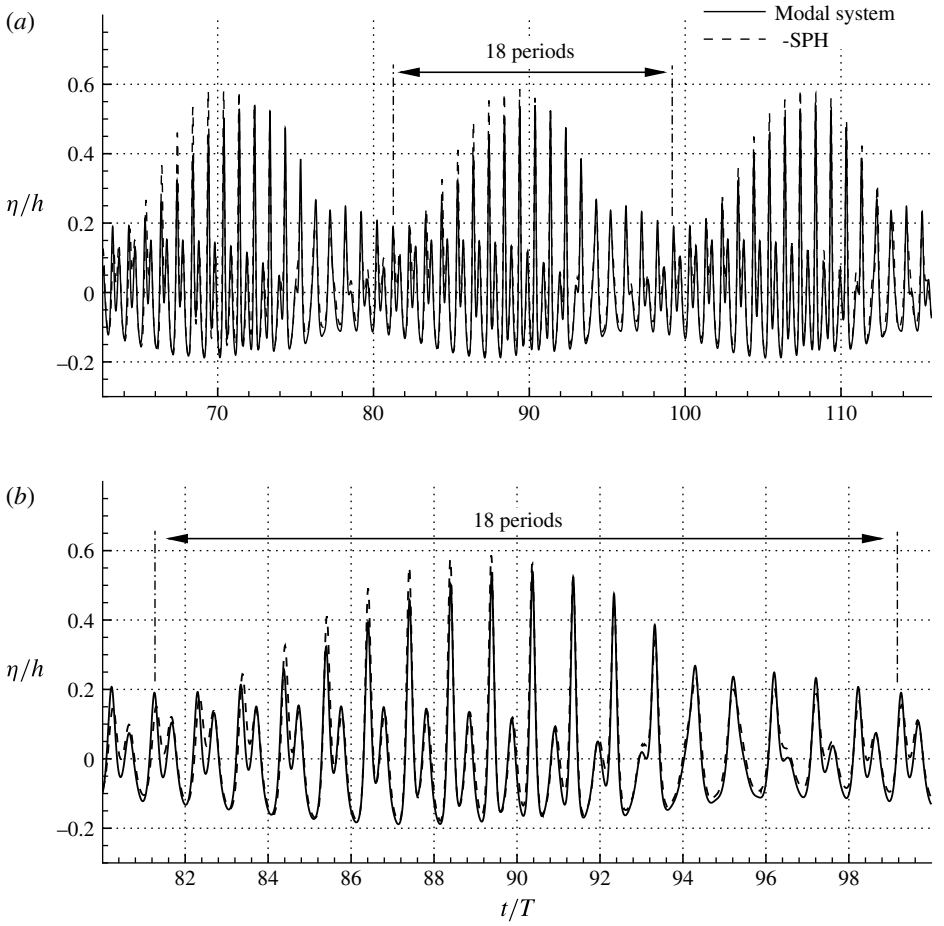

FIGURE 7. Sway motion, second configuration. Evolution of the free surface at $x^*/L^* = 1$ and $\omega/\omega_r = 0.99$, during the 18-period modulation. (*b*) An expanded view of the mid-section of (*a*).

and obtain $\beta_n = 4n^2\pi^2/Re$. Since the global damping rate of the SPH model is $\beta_{sph} = 4\pi^2/Re_{sph}$, a simple and reliable choice is to put $Re = Re_{sph}$ (that is, $\beta_1 = \beta_{sph}$). Specifically, we choose the SPH viscosity of the first sway case (that is, $Re_{sph} = 2900$) and adopt the same tank configuration (see § 3.2). The axis of rotation is displaced at $\boldsymbol{r}_0 = (1/2, 0)$ while the maximum angle of rotation is $\theta_0 = \pi/720$ rad. Since the roll motion generally induces stronger dynamics, a larger number of modes (60 modes) is needed to reach a converged solution. Similarly to the sway cases, all simulations have been run up to $t^*/T^* = 200$ to ensure the attainment of steady-state conditions.

Figure 8(*a*) displays a comparison between the amplitude response operator at $x^*/L^* = 1$ as given by the δ-SPH model (diamonds and thin solid line, $h/\mathrm{d}x = 50$) and by the present model (thick solid line). In this case, the SPH scheme highly overestimates the present model. This is due to the fact that the modal system always predicts $\eta_x = 0$ at the tank ends while in real sloshing phenomena the free-surface profile along walls is characterized by a sharp and thin edge of fluid. The SPH model, because of its Lagrangian structure, is capable of describing this behaviour

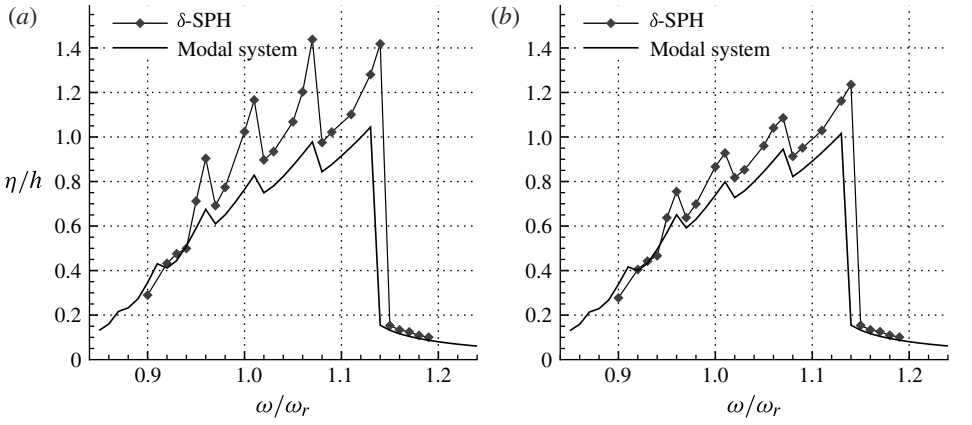

FIGURE 8. Roll motion, response amplitude operator at (*a*) $x^*/L^* = 1$ and (*b*) $x^*/L^* = 0.99$.

even though it generally tends to overpredict the run-up at the walls. This phenomenon has already been observed for the second configuration of the sway motion: figure 5 clearly shows that the SPH outputs (*b*) overestimates the experimental data (*a*). In addition to these considerations, we highlight that the data at tank ends have only a minor influence on the global motion since the fluid edge is very localized in space and time. This is proved in figure 8(*b*) where the amplitude response operator at $x^*/L^* = 0.99$ is displayed. In this case the agreement between the models greatly improves even though the SPH still overestimates the modal system. Note that the response predicted by the modal system is almost unchanged while that given by the SPH strongly reduces due to the absence of the thin fluid edge at the tank ends.

Similarly to the first configuration of the sway motion (see § 3.2), several wave regimes are observed. These spread from four-wave patterns for lower frequencies up to a single-bump wave close to the bifurcation. An overview of this behaviour is provided in figure 9 where the evolution of the free surface is shown at $x^*/L^* = 0.99$. Apart from the slight overestimation of the SPH model, the agreement between the time histories of the free surface is good.

3.4. *General two-dimensional motion*

To prove that the present model is capable of describing a generic two-dimensional motion, we consider a sloshing problem in which sway, roll and heave motion are involved. Incidentally, we note that a similar two-dimensional motion has also been studied in Ardakani & Bridges (2011*a*) by using a model based on the nonlinear shallow-water equations.

The tank dimensions and filling height are the same as the first configuration used by Lepelletier & Raichlen and the tank motion is given by

$$\left.\begin{aligned} &x^*(t^*) = A_1^* \sin(\omega_1^* t^* + \phi_1), \quad y^*(t^*) = A_2^* \sin(\omega_2^* t^* + \phi_2), \\ &\theta(t^*) = \theta_0 \sin(\omega_0^* t^* + \phi_0), \end{aligned}\right\} \tag{3.6}$$

where $A_1^* = 0.006$ m, $\omega_1^* = 2.2$ s^{-1}, $\phi_1 = 0$ (sway motion), $A_2^* = 0.03$ m, $\omega_2^* = 4.29$ s^{-1}, $\phi_2 = 0$ (heave motion), and $\theta_0 = \pi/720$ rad, $\omega_0^* = 0.22$ s^{-1}, $\phi_0 = 0$ (roll motion). Similarly to the roll case described in the previous section, the axis of rotation is placed at $\boldsymbol{r}_0 = (1/2, 0)$. To avoid an impulsive start and make the motion more general,

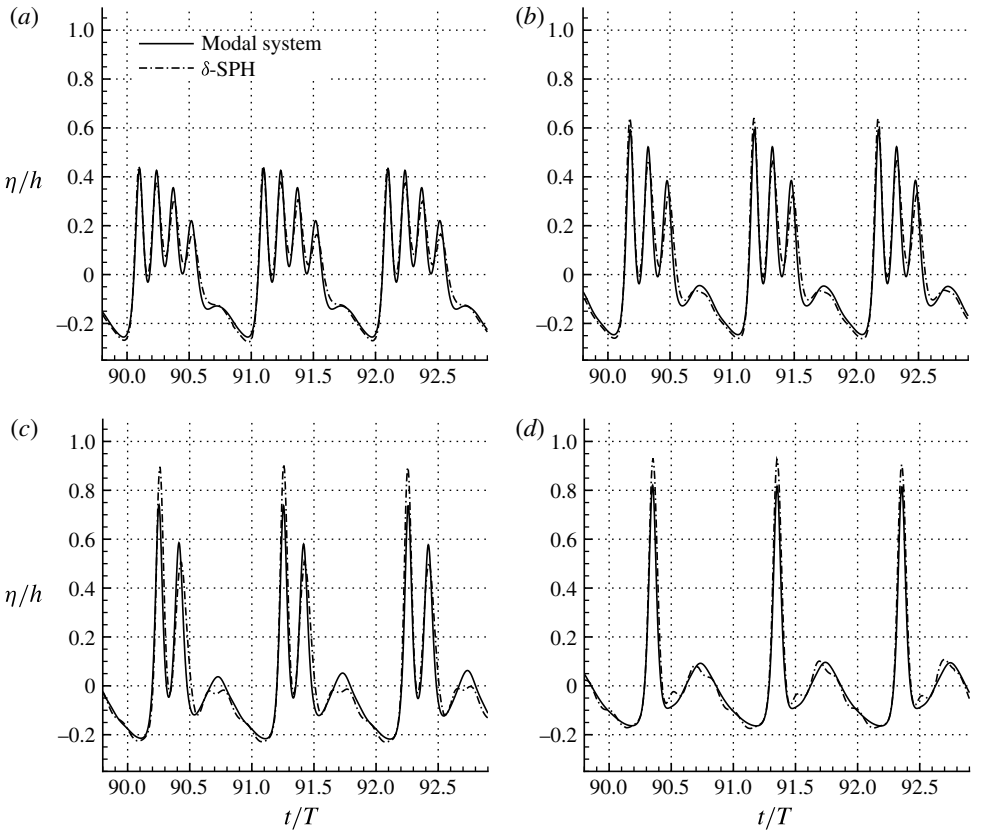

FIGURE 9. Roll motion. Evolution of the free surface at $x^*/L^* = 0.99$: (*a*) $\omega/\omega_r = 0.93$, (*b*) $\omega/\omega_r = 0.97$, (*c*) $\omega/\omega_r = 1.02$, (*d*) $\omega/\omega_r = 1.08$.

we introduce a polynomial ramp during the early stages of the tank evolution. This is given by

$$r(\tau) = \tau^3(6\tau^2 - 15\tau + 10), \tag{3.7}$$

where $\tau = (t^* - t_0^{*(r)})/\Delta t^*$, $t_0^{*(r)}$ is the instant when the ramp is firstly applied ($t_0^{*(r)}$ has been set equal to the initial time of the simulation) and Δt^* is the ramp duration (here $\Delta t^* = 2\pi/\omega_0^*$). The polynomial ramp satisfies

$$r(0) = \dot{r}(0) = \ddot{r}(0) = 0, \quad r(1) = 1, \quad \dot{r}(1) = \ddot{r}(1) = 0, \tag{3.8}$$

so that the initial application of the ramp and its transition towards the imposed motion is perfectly smooth. Similarly to the roll test case, 60 modes are needed to reach a converged solution and the simulation have been run up to $t^*/T^* = 200$ to ensure the attainment of steady-state conditions ($T^* = 2\pi/\omega_0^*$).

Figure 10 displays a comparison between the present model and the SPH outputs ($h/\mathrm{d}x = 50$, $Re = Re_{sph} = 2900$). Similarly to the roll test case, the free-surface signal is recorded at $x^*/L^* = 0.99$ to avoid the overestimation of the SPH due to the thin edge of fluid at the tank wall. Figure 10(*a*,*b*,*c*) displays respectively the initial transitory stage, the steady-state condition and a detail of the steady-state motion. In

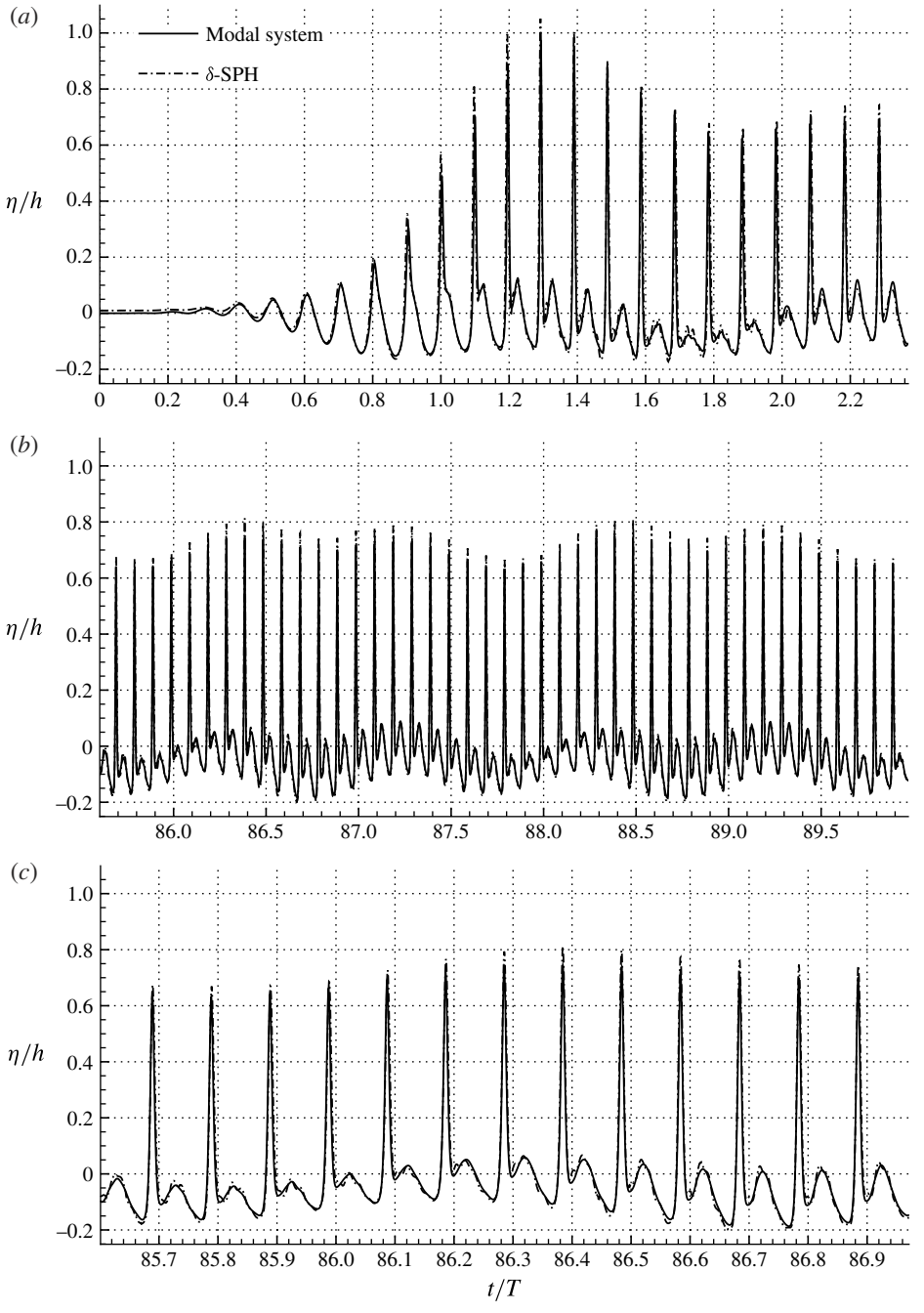

FIGURE 10. General two-dimensional motion. Evolution of the free surface at $x^*/L^* = 0.99$. (*a*) The early stages of the evolution. (*b*) The steady state. (*c*) A detail of the steady-state evolution.

all the cases, the agreement between the modal system (2.14) and the δ-SPH scheme is very good and further proves the accuracy of the present model.

4. Conclusions

A modal system for the analysis of shallow-water sloshing phenomena has been defined starting with a set of Boussinesq-type equations with a linearized dispersive term. This system is based on a spatial Fourier decomposition and is capable of representing a generic two-dimensional motion of the tank. The use of a spatial modulating term allows the simple and straightforward inclusion of the exciting forces inside the modal system and leads to a formulation that is consistent with the conservation of momentum and energy of the flow. Similarly to Ardakani & Bridges (2011*a*), the analysis in appendix A highlights that both sway and roll motions have to be of $O(\mu)$ to be consistent with the shallow-water regime. These bounds, along with the condition that no breaking occurs, fix the limit of applicability of the modal analysis for small filling heights.

Comparisons with both experimental measurements and numerical simulations proved the proposed model to be robust, accurate and capable of describing the main features of the sloshing phenomenon. Further, this confirms that depth-averaged equations (like the Boussinesq-type equations adopted in the present work) can provide a good description of sloshing motions when the water depth is shallow and when waves are non-breaking.

A remarkable advantage of the use of the modal system in comparison with the SPH solver is the much lower computational cost required. This suggests that the modal system may be preferable when there is no need to explicitly compute pressure loads against structures and/or other local quantities.

Further studies will be devoted to the extension of the proposed modal scheme to three-dimensional problems.

Acknowledgements

The research leading to these results has received funding from the European Community's Seventh Framework Programme (FP7/2007-2013) under grant agreement n. 225967 'NextMuSE'. This work was also partially supported by the Centre of Excellence for Ship and Ocean Structures of NTNU Trondheim (Norway) within the 'Violent Water-Vessel Interactions and Related'.

Appendix A. Dynamical forces

Let us consider a frame of reference moving with the tank and with the origin centred at the point of application of the rotation. We denote this frame of reference $x'O'y'$ while we use $x''O''y''$ for the frame of reference fixed with respect to the Earth (see figure 11). The relation between the acceleration of a point in the fixed frame of reference ($\boldsymbol{a}^{*\prime\prime}$) and of a point in the moving one ($\boldsymbol{a}^{*\prime}$) is

$$\boldsymbol{a}^{*\prime\prime} = \boldsymbol{a}^{*\prime} + \boldsymbol{a}_0^{*} + \dot{\boldsymbol{\Omega}}^{*} \times \boldsymbol{r}^{*\prime} + \boldsymbol{\Omega}^{*} \times (\boldsymbol{\Omega}^{*} \times \boldsymbol{r}^{*\prime}) + 2\boldsymbol{\Omega}^{*} \times \boldsymbol{v}^{*\prime}, \tag{A 1}$$

where $\boldsymbol{r}^{*\prime}$ and $\boldsymbol{v}^{*\prime}$ are the position and the velocity vector of a point in the moving frame of reference, $\boldsymbol{\Omega}^{*}$ is the instantaneous angular velocity of the moving frame of reference with respect to the fixed one and $\boldsymbol{a}_0^{*}$ is the translational acceleration of the moving frame of reference with respect to the fixed one. Assuming $\boldsymbol{a}^{*\prime\prime} = \boldsymbol{g}^{*}$, we immediately get

$$\boldsymbol{a}^{*\prime} = \boldsymbol{g}^{*} - \boldsymbol{a}_0^{*} - \dot{\boldsymbol{\Omega}}^{*} \times \boldsymbol{r}^{*\prime} - \boldsymbol{\Omega}^{*} \times (\boldsymbol{\Omega}^{*} \times \boldsymbol{r}^{*\prime}) - 2\boldsymbol{\Omega}^{*} \times \boldsymbol{v}^{*\prime}. \tag{A 2}$$

Let us consider the integral equation for the motion of an incompressible fluid in the moving frame of reference:

$$\int_{V^*} \frac{\mathrm{D}\boldsymbol{v}^{*\prime}}{\mathrm{D}t^*}\,\mathrm{d}V^* = \int_{V^*} \boldsymbol{a}^{*\prime}\,\mathrm{d}V^* + \int_{S^*} \frac{\boldsymbol{\tau}^*}{\rho^*}\,\mathrm{d}S^*, \tag{A 3}$$

where V^* is the volume of the fluid, S^* is the surface of V^* and $\boldsymbol{\tau}^*$ represents the surface forces. The first integral on the right-hand side takes into account the mass forces on the fluid. It is easy to show that

$$\int_{V^*} \boldsymbol{a}^{*\prime}\,\mathrm{d}V^* = \left(\boldsymbol{g}^* - \boldsymbol{a}_0^* - \dot{\boldsymbol{\Omega}}^* \times \boldsymbol{r}_C^{*\prime} - \boldsymbol{\Omega}^* \times (\boldsymbol{\Omega}^* \times \boldsymbol{r}_C^{*\prime}) - 2\boldsymbol{\Omega}^* \times \boldsymbol{v}_C^{*\prime}\right) V^*, \tag{A 4}$$

where $\boldsymbol{r}_C^{*\prime}$ is the centre of mass of the fluid body and $\boldsymbol{v}_C^{*\prime}$ is its velocity, that is

$$\boldsymbol{r}_C^{*\prime} \equiv \frac{1}{V^*}\int_{V^*} \boldsymbol{r}^{*\prime}\,\mathrm{d}V^*, \quad \boldsymbol{v}_C^{*\prime} \equiv \frac{1}{V^*}\int_{V^*} \boldsymbol{v}^{*\prime}\,\mathrm{d}V^*. \tag{A 5}$$

Such a formulation allows rewriting the whole contribution in the following way:

$$\int_{V^*} \boldsymbol{a}^{*\prime}\,\mathrm{d}V^* = \int_{V^*} (\boldsymbol{g}^* - \boldsymbol{a}_0^* - \dot{\boldsymbol{\Omega}}^* \times \boldsymbol{r}_C^{*\prime} - \boldsymbol{\Omega}^* \times (\boldsymbol{\Omega}^* \times \boldsymbol{r}_C^{*\prime}) - 2\boldsymbol{\Omega}^* \times \boldsymbol{v}_C^{*\prime})\,\mathrm{d}V^*. \tag{A 6}$$

Then, in the moving frame of reference (that is, $x'O'y'$), the global mass force is

$$\boldsymbol{F}^{*\prime} = \boldsymbol{g}^* - \boldsymbol{a}_0^* - \dot{\boldsymbol{\Omega}}^* \times \boldsymbol{r}_C^{*\prime} - \boldsymbol{\Omega}^* \times (\boldsymbol{\Omega}^* \times \boldsymbol{r}_C^{*\prime}) - 2\boldsymbol{\Omega}^* \times \boldsymbol{v}_C^{*\prime}. \tag{A 7}$$

When expression (A 7) is written in the frame of reference of the tank (that is, xOy), we, finally, obtain

$$\boldsymbol{F}^* = \boldsymbol{g}^* - \boldsymbol{a}_0^* - \dot{\boldsymbol{\Omega}}^* \times (\boldsymbol{r}_C^* - \boldsymbol{r}_0^*) - \boldsymbol{\Omega}^* \times (\boldsymbol{\Omega}^* \times (\boldsymbol{r}_C^* - \boldsymbol{r}_0^*)) - 2\boldsymbol{\Omega}^* \times \boldsymbol{v}_C^*, \tag{A 8}$$

where $\boldsymbol{r}_C^*$ and $\boldsymbol{v}_C^*$ are the position and the velocity of the mass centre in xOy while $\boldsymbol{r}_0^*$ is the point where the rotation is applied. Consistently with the scaling in (2.2):

$$\boldsymbol{F}^* = g^*\boldsymbol{F}, \quad \boldsymbol{a}_0^* = g^*\boldsymbol{a}_0, \quad \boldsymbol{\Omega}^* = \frac{\sqrt{g^*h^*}}{L^*}\boldsymbol{\Omega}, \quad \boldsymbol{r}^* = L^*\boldsymbol{r}, \quad \boldsymbol{v}^* = \sqrt{g^*h^*}\boldsymbol{v}, \tag{A 9}$$

and, consequently, the dimensionless form of (A 8) is

$$\boldsymbol{F} = \hat{\boldsymbol{g}} - \boldsymbol{a}_0 - \mu\dot{\boldsymbol{\Omega}} \times (\boldsymbol{r}_C - \boldsymbol{r}_0) - \mu\boldsymbol{\Omega} \times (\boldsymbol{\Omega} \times (\boldsymbol{r}_C - \boldsymbol{r}_0)) - 2\mu\boldsymbol{\Omega} \times \boldsymbol{v}_C. \tag{A 10}$$

Here, $\hat{\boldsymbol{g}}$ indicates the unit vector pointing in the same direction as $\boldsymbol{g}^*$.

Now, we rewrite (A 10) in two dimensions. Because of the scaling in (2.2), the vertical components of $\boldsymbol{r}$ and $\boldsymbol{v}$ are of $O(\mu)$. Then, $\boldsymbol{r}_C = (x_C, \mu y_C, 0)$, $\boldsymbol{v}_C = (u_C, \mu v_C, 0)$. Further, we denote $\boldsymbol{a}_0 = (a_{0,1}, a_{0,2}, 0)$ and $\boldsymbol{\Omega} = (0, 0, \dot{\theta})$ where θ is the angle of the horizontal axis of $x'O'y'$ with respect to the horizontal axis of $x''O''y''$ (see figure 11). Then, (A 10) gives

$$\begin{aligned} F_1(t) = &-\sin\theta - a_{0,1}\cos\theta - a_{0,2}\sin\theta + \mu^2\ddot{\theta}(y_C - y_0) \\ &+ \mu\dot{\theta}^2(x_C - x_0) + 2\mu^2\dot{\theta}v_C, \end{aligned} \tag{A 11}$$

$$\begin{aligned} F_2(t) = &-\cos\theta + a_{0,1}\sin\theta - a_{0,2}\cos\theta - \mu\ddot{\theta}(x_C - x_0) \\ &+ \mu^2\dot{\theta}^2(y_C - y_0) - 2\mu\dot{\theta}u_C. \end{aligned} \tag{A 12}$$

The horizontal component, $F_1(t)$, has to be added as a forcing term to the momentum equation of the Boussinesq model. Conversely, the vertical component, $F_2(t)$, becomes a multiplicative factor for η_x.

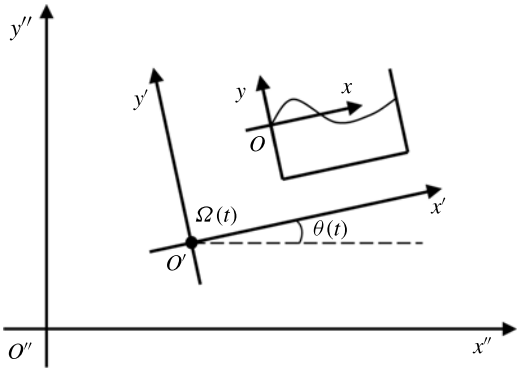

FIGURE 11. Sketch of the fixed frame of reference ($x''O''y''$), of the moving one ($x'O'y'$) and of the frame of reference of the tank (xOy).

Note that the forcing term of (2.5) is F_1/μ. Then, to avoid singularity in the shallow-water limit (that is, for μ going to zero), we must have

$$a_{0,1} = O(\mu), \quad \theta = O(\mu). \tag{A 13}$$

These bounds imply some restrictions on sway and roll motions for sloshing phenomena in shallow-water conditions (see for example Ardakani & Bridges 2011*a*).

A.1. *Details of computation*

To evaluate the forcing term in (A 8), we need to compute the position and velocity of the mass centre. Using the first definition in (A 5), we get

$$x_C^* = \frac{1}{V^*}\int_0^{L^*} x^*\,\mathrm{d}x^* \int_{-h^*}^{\eta^*} \mathrm{d}z^*, \quad y_C^* = \frac{1}{V^*}\int_0^{L^*} \mathrm{d}x^* \int_{-h^*}^{\eta^*} z^*\,\mathrm{d}z^*. \tag{A 14}$$

Since the fluid is incompressible, the total volume of water is constant and equal to h^*L^*. Then, using the first expression of (2.6), it is simple to show that:

$$x_C^* = L^*\left\{\frac{1}{2} + \sum_{n=1}^{+\infty} \frac{[-1+(-1)^n]}{\pi^2 n^2}\frac{H_n^*(t^*)}{h^*}\right\}, \tag{A 15}$$

$$y_C^* = h^*\left\{-\frac{1}{2} + \sum_{n=1}^{+\infty} \left[\frac{H_n^*(t^*)}{2h^*}\right]^2\right\}. \tag{A 16}$$

The mass-centre velocity is simply given by the time derivative of the mass-centre position:

$$u_C^* = L^*\sum_{n=1}^{+\infty} \frac{[-1+(-1)^n]}{\pi^2 n^2}\frac{\dot{H}_n^*(t^*)}{h^*}, \tag{A 17}$$

$$v_C^* = \sum_{n=1}^{+\infty} \frac{H_n^*(t^*)}{2h^*}\dot{H}_n^*(t^*). \tag{A 18}$$

Finally, the forcing term is completely known when $\boldsymbol{\Omega}^*$, $\boldsymbol{r}_0^*$ and $\boldsymbol{a}_0^*$ are assigned.

Appendix B. The modulating term

In this appendix we prove that the modulating term, $M(x)$, has to be expressed as a series of sines (see (2.9)). This is a consequence of the use of the Fourier series (2.6)–(2.7) and of the symmetries of system (2.5).

Let us consider system (2.5) and substitute expansion (2.7) in the momentum equation. We find

$$\sum_{n\in\mathbb{Z}}\left[\dot{U}_n\left(1+\frac{\pi^2\mu^2n^2}{3}\right)+n\pi F_2H_n+\frac{n\pi}{4}\sum_{p\in\mathbb{Z}}U_pU_{n-p}\right]\mathrm{e}^{\mathrm{i}n\pi x}=2\mathrm{i}F_1. \tag{B 1}$$

To include the forcing inside the summation, we assume F_1 to be multiplied by a modulating term $M(x)$ that is expanded in a series as follows:

$$M(x)=\sum_{n\in\mathbb{Z}}\frac{M_n}{2\mathrm{i}}\exp(\mathrm{i}n\pi x). \tag{B 2}$$

Then, we obtain

$$\dot{U}_n\left(1+\frac{\pi^2\mu^2n^2}{3}\right)+n\pi F_2H_n+\frac{n\pi}{4}\sum_{p\in\mathbb{Z}}U_pU_{n-p}=M_nF_1. \tag{B 3}$$

The modulating amplitude M_n must satisfy some symmetry conditions. To find them, we consider the modal equation for the mode $-n$, that is

$$\dot{U}_{-n}\left(1+\frac{\pi^2\mu^2n^2}{3}\right)-n\pi F_2H_{-n}-\frac{n\pi}{4}\sum_{p\in\mathbb{Z}}U_pU_{-n-p}=M_{-n}F_1. \tag{B 4}$$

Since $U_n=-U_{-n}$ and $H_n=H_{-n}$, this equation becomes

$$\dot{U}_n\left(1+\frac{\pi^2\mu^2n^2}{3}\right)+n\pi F_2H_n+\frac{n\pi}{4}\sum_{p\in\mathbb{Z}}U_pU_{-n-p}=-M_{-n}F_1. \tag{B 5}$$

Now, let us focus on the nonlinear term. It can be rewritten as follows:

$$\sum_{p\in\mathbb{Z}}U_pU_{-n-p}=\sum_{p\in\mathbb{Z}}U_{-p}U_{-n+p}=\sum_{p\in\mathbb{Z}}U_pU_{n-p}, \tag{B 6}$$

and, therefore, (B 5) becomes

$$\dot{U}_n\left(1+\frac{\pi^2\mu^2n^2}{3}\right)+n\pi F_2H_n+\frac{n\pi}{4}\sum_{p\in\mathbb{Z}}U_pU_{n-p}=-M_{-n}F_1. \tag{B 7}$$

Comparing (B 7) and (B 3) we find

$$M_n=-M_{-n}\quad\Rightarrow\quad M(x)=\sum_{n=1}^{+\infty}M_n\sin(n\pi x). \tag{B 8}$$

This proves the validity of the expansion in (2.9).

B.1. *Conservation properties*

For consistency with the governing equations, the modulating term must approximate unity, that is, $M(x)\simeq 1$. This corresponds to

$$M_n=-2\left[\frac{(-1)^n-1}{n\pi}\right]\quad\text{for } n\in\mathbb{Z}\setminus\{0\},\quad M_0=0. \tag{B 9}$$

Since $M(x)$ must not modify the global action of F_1 on the governing equations, we have to check that the integral equations of the momentum and energy remain unchanged. Since the Boussinesq equations are depth-averaged and $D^* \ll L^*$, this is equivalent to checking whether the following one-dimensional integral relations hold:

$$\int_0^1 F_1(t)M(x)\,\mathrm{d}x = F_1(t)\int_0^1 M(x)\,\mathrm{d}x = F_1(t), \tag{B 10}$$

$$\int_0^1 u(x,t)F_1(t)M(x)\,\mathrm{d}x = F_1(t)\int_0^1 u(x,t)M(x)\,\mathrm{d}x = F_1(t)\int_0^1 u(x,t)\,\mathrm{d}x, \tag{B 11}$$

that is

$$\int_0^1 M(x)\,\mathrm{d}x = 1, \quad \int_0^1 u(x,t)M(x)\,\mathrm{d}x = \int_0^1 u(x,t)\,\mathrm{d}x. \tag{B 12}$$

The first relation comes from the integration of the momentum equation of system (2.5) while the second has been derived by integrating the corresponding energy equation, that is, the momentum equation of system (2.5) multiplied by u. Let us focus on the first relation of (B 12). Using the first expression in (2.9), it follows that

$$\int_0^1 M(x)\,\mathrm{d}x = \frac{2}{\pi^2}\sum_{n=1}^{+\infty}\frac{[(-1)^n-1]^2}{n^2} = \frac{4}{\pi^2}\sum_{n=1}^{+\infty}\frac{[1-(-1)^n]}{n^2}. \tag{B 13}$$

Since the summations on the right-hand side give

$$\sum_{n=1}^{+\infty}\frac{1}{n^2} = \frac{\pi^2}{6}, \quad \sum_{n=1}^{+\infty}\frac{(-1)^n}{n^2} = -\frac{\pi^2}{12}, \tag{B 14}$$

the first relation of (B 12) is satisfied. Now let focus on the second equation in (B 12). Using (2.6) and (B 9), we obtain

$$\int_0^1 u(x,t)\,\mathrm{d}x = -\frac{1}{\pi}\sum_{n=1}^{\infty}U_n\frac{[(-1)^n-1]}{n}, \tag{B 15}$$

$$\int_0^1 u(x,t)M(x)\,\mathrm{d}x = -\frac{2}{\pi}\sum_{p,q=1}^{\infty}U_p\frac{[(-1)^q-1]}{q}\int_0^1 \sin(p\pi x)\sin(q\pi x)\,\mathrm{d}x. \tag{B 16}$$

Since

$$\int_0^1 \sin(p\pi x)\sin(q\pi x)\,\mathrm{d}x = \tfrac{1}{2}\delta_{pq}, \tag{B 17}$$

the second relation of (B 12) is satisfied.

REFERENCES

ANTUONO, M., COLAGROSSI, A., MARRONE, S. & LUGNI, C. 2011 Propagation of gravity waves through SPH schemes with numerical diffusive terms. *Comput. Phys. Commun.* **182**, 866–877.

ANTUONO, M., COLAGROSSI, A., MARRONE, S. & MOLTENI, D. 2010 Free-surface flows solved by means of SPH schemes with numerical diffusive terms. *Comput. Phys. Commun.* **181** (3), 532–549.

ARDAKANI, H. A. & BRIDGES, T. J. 2011*a* Shallow-water sloshing in vessels undergoing prescribed rigid-motion in two dimensions. *Eur. J. Mech.* B/*Fluids* **31**, 40–43.

ARDAKANI, H. A. & BRIDGES, T. J. 2011*b* Shallow-water sloshing in vessels undergoing prescribed rigid-motion in three dimensions. *J. Fluid Mech.* **667**, 474–519.

BOUSCASSE, B., COLAGROSSI, A., COLICCHIO, G. & LUGNI, C. 2007 Numerical and experimental investigation of sloshing phenomena in conditions of low filling ratios. In *10th Numerical Towing Tank Symposium (NuTTS'07) Hamburg, Germany, 23–25 Sep. 2009*. Curran Associates, Inc.

BULIAN, G., SOUTO-IGLESIAS, A., DELORME, L. & BOTIA-VERA, E. 2010 Smoothed particle hydrodynamics (SPH) simulation of a tuned liquid damper. *J. Hydraul. Res.* **48** (1), 28–39.

COLAGROSSI, A., COLICCHIO, G., LUGNI, C. & BROCCHINI, M. 2010 A study of violent sloshing wave impacts using an improved SPH method. *J. Hydraul. Res.* **48**, 94–104.

ESPAÑOL, P. & REVENGA, M. 2003 Smoothed dissipative particle dynamics. *Phys. Rev.* E **67**, 026705-1:12.

FALTINSEN, O. M. 2005 *Hydrodynamics of High-Speed Marine Vehicles*. Cambridge University Press.

FALTINSEN, O. M., ROGNEBAKKE, O. F., LUKOVSKY, I. A. & TIMOKHA, A. N. 2000 Multidimensional modal analysis of nonlinear sloshing in a rectangular tank with finite water depth. *J. Fluid Mech.* **407**, 201–234.

FALTINSEN, O. M., ROGNEBAKKE, O. F. & TIMOKHA, A. N. 2006 Transient and steady-state amplitudes of resonant three-dimensional sloshing in a square base tank with a finite fluid depth. *Phys. Fluids* **18**, 012103 1–14.

FALTINSEN, O. M. & TIMOKHA, A. N. 2001 An adaptive multimodal approach to nonlinear sloshing in a rectangular tank. *J. Fluid Mech.* **432**, 167–200.

FALTINSEN, O. M. & TIMOKHA, A. N. 2002 Asymptotic modal approximation of nonlinear resonant sloshing in a rectangular tank with small fluid depth. *J. Fluid Mech.* **470**, 319–357.

FALTINSEN, O. M. & TIMOKHA, A. N. 2009 *Sloshing*. Cambridge University Press.

GOBBI, M. F., KIRBY, J. T. & WEI, G. 2000 A fully nonlinear Boussinesq model for surface waves. Part 2. Extension to $O(k\mu)^4$. *J. Fluid Mech.* **405**, 181–210.

HILL, D. F. 2003 Transient and steady-state amplitudes of forced waves in rectangular basins. *Phys. Fluids* **39** (6), 1576–1587.

KEULEGAN, G. H. 1959 Energy dissipation in standing waves in rectangular basins. *J. Fluid Mech.* **6**, 33–50.

LAMB, H. 1945 *Hydrodynamics*. Cambridge University Press.

LANDRINI, M., COLAGROSSI, A., GRECO, M. & TULIN, M. P. 2007 Gridless simulations of splashing processes and near-shore bore propagation. *J. Fluid Mech.* **591**, 183–213.

LEPELLETIER, T. G. & RAICHLEN, F. 1988 Nonlinear oscillations in rectangular tanks. *J. Engng Maths* **114** (1), 1–23.

LIGHTHILL, J. 2001 *Waves in Fluids*. Cambridge University Press.

LUGNI, C., BROCCHINI, M. & FALTINSEN, O. M. 2006 Wave impact loads: the role of the flip-through. *Phys. Fluids* **18**, 122101:1–17.

LUGNI, C., BROCCHINI, M. & FALTINSEN, O. M. 2010*a* Evolution of the air cavity during a depressurized wave impact. II. The dynamic field. *Phys. Fluids* **22**, 056102:1–13.

LUGNI, C., MIOZZI, M., BROCCHINI, M. & FALTINSEN, O. M. 2010*b* Evolution of the air cavity during a depressurized wave impact. I. The kinematic flow field. *Phys. Fluids* **22**, 056101:1–17.

MADSEN, P. A., BINGHAM, H. B. & LIU, H. 2002 A new Boussinesq method for fully nonlinear waves from shallow to deep water. *J. Fluid Mech.* **462**, 1–30.

MADSEN, P. A. & SHÄFFER, H. A. 2006 A discussion of artificial compressibility. *Coast. Engng* **53**, 93–98.

MARRONE, S., ANTUONO, M., COLAGROSSI, A., COLICCHIO, G., TOUZÉ, D. LE & GRAZIANI, G. 2011 δ-SPH model for simulating violent impact flows. *Comput. Meth. Appl. Mech. Engng* **200**, 1526–1542.

MARRONE, S., COLAGROSSI, A., TOUZÉ, D. LE & GRAZIANI, G. 2010 Fast free-surface detection and level-set definition in SPH solvers. *J. Comput. Phys.* **229**, 3652–3663.

MONAGHAN, J. J. 2005 Smoothed particle hydrodynamics. *Rep. Prog. Phys.* **68**, 1703–1759.

NWOGU, O. 1993 Alternative form of Boussinesq equations for nearshore wave propagation. *J. Waterways Port Coast. Ocean Engng* **119**, 618–638.

OCKENDON, H., OCKENDON, J. R. & JOHNSON, A. D. 1986 Resonant sloshing in shallow water. *J. Fluid Mech.* **167**, 465–479.

OLSEN, H. & JOHNSEN, K. 1975 Nonlinear sloshing in rectangular tanks: a pilot study on the applicability of analytical models. *Tech. Rep.* 74-72-5 Vol. 2. Det Norske Veritas (DNV), Hvik, Norway.

PANTAZOPOULOS, M. 1987 Numerical solution of the general shallow water sloshing problem. PhD thesis, University of Washington, Seattle.

RANDLES, P. W. & LIBERSKY, L. D. 1996 Smoothed particle hydrodynamics: Some recent improvements and applications. *Comput. Meth. Appl. Mech. Engng* **139**, 375–408.

SOUTO-IGLESIAS, A., DELORME, L., PÉREZ-ROJAS, L. P. & ABRIL-PÉREZ, S. 2006 Liquid moment amplitude assessment in sloshing type problems with smooth particle hydrodynamics. *Ocean Engng* **33** (11), 1462–1484.

VEERAMONY, J. & SVENDSEN, I. A. 2000 The flow in surf-zone waves. *Coast. Engng* **39**, 93–122.

WHITHAM, G. B. 1974 *Linear and Nonlinear Waves*. John Wiley & Sons.